NANO LETTERS
Letter
Cite This: Nano Lett. 2018, 18, 2870−2878
pubs.acs.org/NanoLett

Tuning Nanocrystal Surface Depletion by Controlling Dopant Distribution as a Route Toward Enhanced Film Conductivity

Corey M. Staller,[†] Zachary L. Robinson,[‡] Ankit Agrawal,[†] Stephen L. Gibbs,[†] Benjamin L. Greenberg,[§] Sebastien D. Lounis,[∥,⊥] Uwe R. Kortshagen,[§] and Delia J. Milliron*[,†]

[†]McKetta Department of Chemical Engineering, University of Texas at Austin, Austin, Texas 78712-1589, United States
[‡]Department of Physics, University of Minnesota, Minneapolis, Minnesota 55455, United States
[§]Department of Mechanical Engineering, University of Minnesota, Minneapolis, Minnesota 55455, United States
[∥]The Molecular Foundry, Lawrence Berkeley National Laboratory, 1 Cyclotron Road, Berkeley, California 94720, United States
[⊥]Graduate Group in Applied Science and Technology, University of California, Berkeley, Berkeley, California 94720, United States

Supporting Information

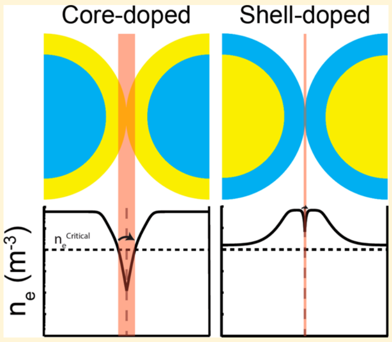

ABSTRACT: Electron conduction through bare metal oxide nanocrystal (NC) films is hindered by surface depletion regions resulting from the presence of surface states. We control the radial dopant distribution in tin-doped indium oxide (ITO) NCs as a means to manipulate the NC depletion width. We find in films of ITO NCs of equal overall dopant concentration that those with dopant-enriched surfaces show decreased depletion width and increased conductivity. Variable temperature conductivity data show electron localization length increases and associated depletion width decreases monotonically with increased density of dopants near the NC surface. We calculate band profiles for NCs of differing radial dopant distributions and in agreement with variable temperature conductivity fits find NCs with dopant-enriched surfaces have narrower depletion widths and longer localization lengths than those with dopant-enriched cores. Following amelioration of NC surface depletion by atomic layer deposition of alumina, all films of equal overall dopant concentration have similar conductivity. Variable temperature conductivity measurements on alumina-capped films indicate all films behave as granular metals. Herein, we conclude that dopant-enriched surfaces decrease the near-surface depletion region, which directly increases the electron localization length and conductivity of NC films.

KEYWORDS: *Nanocrystal, depletion, dopant distribution, conduction, tin-doped indium oxide, band profile*

Transparent conductive oxide (TCO) thin films are of fundamental importance in the modern world due to their vast application in optoelectronic devices such as displays, solar cells, and electrochromic windows.[1,2] These applications require high conductivity, which has traditionally been achieved through vacuum deposition of amorphous or crystalline doped metal oxide films.[2] An effort to reduce manufacturing cost by moving away from vacuum deposition has motivated research on using films of colloidal nanocrystals (NCs) as TCO films. However, colloidal NCs are synthesized with long chain organic capping ligands resulting in spatial separations between neighboring NCs that act as tunneling barriers.[3−5] Carrier conduction in these systems occurs through a hopping mechanism, which is described by the Miller-Abraham model

$$\sigma \propto A\exp\left(-\frac{2r_{ij}}{a}\right)\exp\left(-\frac{E_{ij}}{k_{B}T}\right)$$

where σ is conductivity, A is a material-dependent constant, r_{ij} is the distance between sites i and j, a is the inverse of the wave function decay rate (called the electron localization length), E_{ij} is the energetic barrier encountered moving from site i to j, k_B is the Boltzmann constant, and T is temperature.[6] Inspection of the Miller-Abraham model leads to two obvious routes to improve NC film conductivity—reducing the distance between sites and lowering the energetic cost of hopping.[7,8]

Many efforts have focused on reducing the distance between NCs to improve electron transport through NC films. Initial work on colloidally synthesized NC films concentrated on exchanging the organic capping ligands used in synthesis with a variety of organic and inorganic ligands of different lengths or bonding arrangements to modify inter-NC charge transfer or hopping.[4,5,9,10] However, NC films with any ligands still in place are often too resistive to be suitable for device applications. Various ligand stripping and decomposition reactions have been developed to improve the conductivity of NC films.[5,11] Removal of ligands from NC surfaces often leads to several orders of magnitude increase in conductivity. While this strategy significantly improves film conductivity, removal of ligands exposes NC surfaces to adventitious chemical species,

Received: December 31, 2017
Revised: April 19, 2018
Published: April 30, 2018

DOI: 10.1021/acs.nanolett.7b05484
Nano Lett. 2018, 18, 2870−2878

such as water that leads to hydroxylation, forming surface states that are difficult to control and can be harmful to charge transport through NC films.

One method to improve conduction through NC films is to use atomic layer deposition (ALD) to cap bare NC arrays with metal oxides, such as alumina (Al_2O_3).[12−16] Specifically, Thimsen et al. found that ZnO NC films with alumina capping layers had conductivity 8 orders of magnitude higher than that of bare films.[13] This approach was later elaborated upon by Ephraim et al., who explained that the significant film performance improvement following alumina deposition is due to the removal of adsorbed water species by trimethylaluminum, the precursor used during alumina ALD.[14] These studies suggest that adsorbed water species play a direct role in affecting film conductivity but the mechanism by which adsorbed water species actually lead to reduced conductivity remains unexplored.[13,17] Recently, Zandi and Agrawal et al. reported that electrochemical modulation of optical absorption in tin-doped indium oxide (ITO) NC films can be explained by the formation of a depletion region near NC surfaces.[17] We can therefore hypothesize that the enhanced electron transport in films whose surface hydroxyls have been eliminated is a result of alleviating depletion effects that were present due to the hydroxyl-associated surface states. Here we examine the role that depletion plays in inhibiting charge transport, and we study how the properties of NCs and their surfaces can be tuned to reduce depletion effects and improve transport.

Specifically, we report the influence of the intra-NC dopant distribution on conductivity of ITO NC films. Films comprised of NCs of similar size and overall tin concentration show a marked difference in film conductivity when the radial dopant distribution is manipulated. Bare NC films of a given overall dopant concentration exhibit higher conductivity, larger electron localization length, and lower contact resistance when dopant concentration is high near the NC surface. The dependence of electronic properties on dopant distribution is understood by examining how the intra-NC band profile is altered by dopant segregation in the presence of a depletion region near the NC surface. Following alumina ALD, films display comparable conductivity and contact resistance, independent of NC dopant profile, confirming that depletion-related resistance plays a dominant role in differentiating the electronic behavior of bare NC films of differing intra-NC dopant profiles.

Experimental Procedures. ITO NCs were synthesized using a two-step method adapted from the slow growth methods developed by Jansons et al.[18] The dopant distribution was controlled by synthesizing ITO NC cores of a desired dopant concentration, which then undergo a washing procedure before reintroduction to a reaction flask for shell growth of desired dopant concentration and shell thickness (see SI Text 1 and Figure S2 for further synthetic details and X-ray diffraction (XRD)). This synthetic method leads to highly controlled core and shell sizes and low size polydispersity. Core and overall particle sizes were measured by Scherrer analysis of the ITO (222) XRD peak and validated by scanning transmission electron microscopy (Figures S1−3). Dopant incorporation was quantified by elemental analysis using inductively coupled plasma-atomic emission spectroscopy (ICP-AES) for overall Sn dopant concentration and X-ray photoelectron spectroscopy (XPS) with an Al K_α source (1486.7 eV) to assess the near-surface Sn dopant concentration (Figure S4). Al K_α source energy corresponds to a photoelectron escape depth of about 1.5 nm.[19]

Colloidal NCs were spin-coated from a concentrated dispersion in a mixed solvent of hexane and octane (1:1) onto silicon and quartz substrates, yielding approximately 100 nm thick films. To enhance electron transport, the organic ligands used in colloidal NC synthesis were removed by an in situ ligand displacement with formic acid followed by a 60 min anneal at 300 °C in flowing nitrogen gas to decompose and desorb the remaining organic matter.[11] Ligand removal was verified by Fourier-transform infrared spectroscopy (Figure S5). The resulting films were highly transparent at visible wavelengths (Figure S6). Scanning electron microscopy (SEM) images show densely packed films with direct contact between NCs and minimal cracking (Figure 1). Porosity of NC films prepared on silicon substrates was determined using ellipsometric porosimetry (EP) with toluene as the dielectric contrast solvent. EP data from 400 to 1000 nm wavelength were fit using software provided by JA Woollam and yielded consistent volume fractions between 0.72 and 0.78 for all films (Figure S7).

To understand the influence of dopant distribution on film electronic properties when surface depletion is suppressed, bare NC films were capped with 40 ALD cycles of alumina deposition to passivate NC surfaces. Deposition was carried out in a Savannah ALD chamber using previously reported methods.[14] Trimethylaluminum was used as the aluminum precursor and deposition was carried out at 180 °C. These conditions correspond to a growth rate of about 0.11 nm per ALD cycle.[13] SEM and time-of-flight secondary ion mass spectrometry (TOF-SIMS) showed 40 cycles of alumina deposition penetrated through the full film thickness and resulted in nearly complete infilling of NC films and deposition of a thin overlayer on the films (Figures S8 and S9). A similar approach was used by Ephraim et al., who reported that deposition of alumina on surface segregated ITO NC films by ALD removes adsorbed water species and yields conductive ITO-alumina composites.[14]

To minimize aberrations in data, all analyses were conducted on samples that were exposed to ambient lab air for at least 23 days (Figure S10). Room-temperature conductivity measurements were collected on an Ecopia Hall Effect measurement system (HMS-5000) in the 4-point probe Van der Pauw geometry. Gold spring-clip contacts were placed directly on the films and edge effects were minimized by isolating a uniform square region in the center of the film using a diamond scribe. Variable temperature conductivity measurements were conducted in a Physical Property Measurement System (PPMS) from as low as 2 K up to 300 K in both decreasing and increasing temperature directions. Ohmic contact was established using indium solder pads. Bare and alumina-capped NC film room-temperature conductivity data represent an average over six and two samples, respectively.

Bare NC Films. To investigate the role that dopant distribution plays in conductivity of ITO films, it was necessary to synthesize a series of NCs with similar size and overall dopant concentration (two properties that are known to affect conductivity)[20−22] but with variations in the radial profile of dopants. More specifically, thanks to unprecedented size and dopant incorporation control afforded by the synthetic methods advanced by Janson et al.,[18] we varied the density of dopants radially within each NC while keeping the overall dopant concentration and NC diameter nearly constant at 3

DOI: 10.1021/acs.nanolett.7b05484
Nano Lett. 2018, 18, 2870−2878

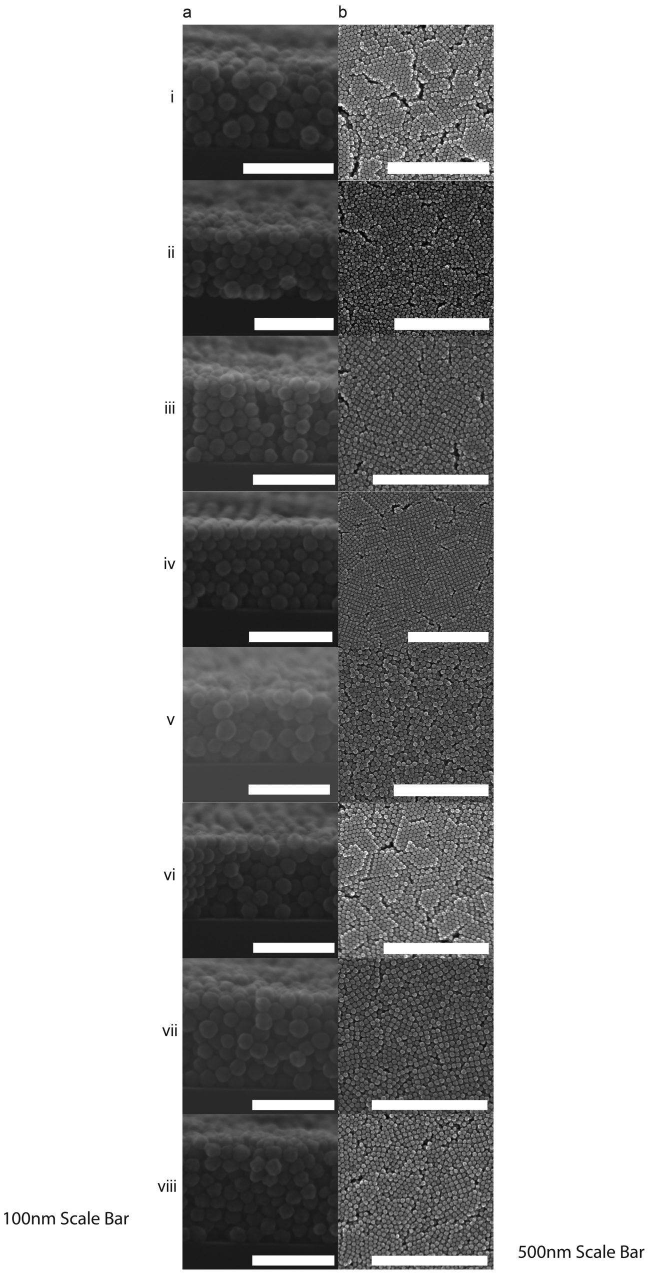

Figure 1. Bare NC film on silicon SEM cross-section (a) and top-down (b) for Core8 (i), Core5 (ii), Core4 (iii), Uniform (iv), Shell4 (v), Shell5 (vi), Shell8A (vii), and Shell8B (viii). Scale bars represent 100 nm for cross-section and 500 nm for top-down.

Table 1. ITO NC Core−Shell Structure[a]

sample	dopant distribution	core diameter (nm)	overall diameter (nm)	atom % Sn by ICP-AES	atom % Sn by XPS
Core8	core-doped	14.4	20.8	3.3 ± 0.2	2.2
Core5	core-doped	16.5	20.8	3.1 ± 0.3	2.4
Core4	core-doped	16.3	19.0	2.7 ± 0.1	2.4
uniform	uniform	16.6	20.2	3.0 ± 0.1	3.9
Shell4	surface-doped	16.4	24.7	3.2 ± 0.1	5.3
Shell5	surface-doped	15.1	20.7	3.1 ± 0.2	6.5
Shell8A	surface-doped	16.6	22.1	3.3 ± 0.1	6.8
Shell8B	surface-doped	16.8	19.8	2.5 ± 0.1	6.3

[a] Core and overall NC sizes by Scherrer analysis, overall tin dopant concentration by ICP-AES, and near-surface tin dopant concentration by XPS.

atom % and 20 nm, respectively. The eight samples investigated here are uniformly doped (Uniform), core-doped with an undoped shell/4 atom % core (Core4), 5 atom % core (Core5), and 8 atom % core (Core8), and shell-doped with an undoped core/4 atom % shell (Shell4), 5 atom % shell (Shell5), 8 atom % shell (Shell8A), and 8 atom % shell at 2.5 atom % overall (Shell8B). NC sizes and dopant profile are summarized in Table 1. Discrepancies between nominal shell dopant concentration and that measured by XPS may be due to moderate redistribution of Sn during NC synthesis. However, the near-surface Sn concentration observed by XPS is unaffected by the ligand removal and annealing processes (Figure S11 and Table S1). Despite this, comparing tin content by XPS and ICP-AES shows significant dopant segregation for all core−shell samples and a clear trend of increasing near-surface dopant concentration from Core8 to Shell8A.

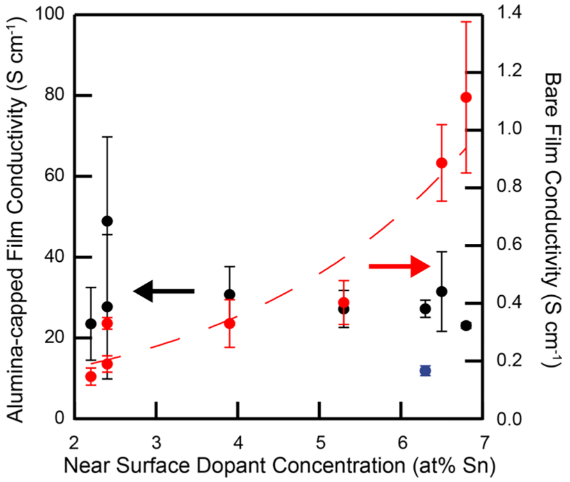

Figure 2. Film conductivity. Room-temperature conductivity for bare ITO NC films of equal overall dopant concentration shows an exponential dependence on the near surface dopant concentration, as measured by XPS. This dependence is not observed in the room-temperature conductivity of alumina-capped ITO NC films. Dashed line shows an exponential fit of bare film conductivity. The blue point represents Shell8B, which was not included in the fit.

We measure conductivity of bare films following prolonged ambient lab air exposure to minimize variations in surface chemistry from sample to sample. Bare film conductivity is shown in Figure 2. Conductivity of all samples of equal overall dopant concentration shows an exponential dependence on the near-surface dopant concentration. Core8 and Core5 exhibit the lowest average conductivity of the series at 0.154 S-cm^{-1} and 0.168 S-cm^{-1}, respectively. As dopants are placed closer to the surface, the conductivity more than doubles upon reaching uniform distribution, where the measured conductivity was 0.343 S-cm^{-1}. Finally, Shell5 and Shell8A show the highest conductivity of the series at 0.901 S-cm^{-1} and 1.11 S-cm^{-1}, respectively, representing a nearly nine-time increase from the lowest conductivity sample, Core8. We note that while Shell8B has a high dopant concentration on the surface, it shows a significantly lower conductivity than expected based on the

Table 2. Localization Length and Contact Resistance[a]

sample	bare			alumina-capped		
	simulated localization length (nm)	localization length (nm)	contact resistance (kΩ)	simulated localization length (nm)	metallic grain size (nm)	contact resistance (kΩ)
Core8	18.2	18.2 ± 1.2	1206 ± 248	≥20.8	25.0 ± 0.4	19.9 ± 0.2
Core5	19.2	18.1 ± 1.1	787 ± 118	≥20.8	22.0 ± 0.4	19.2 ± 0.2
Core4	18.3	16.9 ± 1.6	524 ± 98	≥19.0	19.4 ± 0.7	14.1 ± 0.2
Uniform	19.8	18.5 ± 1.1	443 ± 111	≥20.2	22.1 ± 0.4	20.8 ± 0.1
Shell4	≥24.7	35.0 ± 2.8	288 ± 55	≥24.7	22.7 ± 0.5	25.3 ± 0.2
Shell5	20.6	21.8 ± 1.9	158 ± 24	≥20.7	22.7 ± 0.5	19.8 ± 0.2
Shell8A	≥21.5	33.8 ± 2.4	121 ± 28	≥21.5	22.8 ± 0.5	21.8 ± 0.3
Shell8B	≥19.8	25.1 ± 1.5	1040 ± 106	≥19.8	24.9 ± 0.7	24.0 ± 0.3

[a] Bare films: localization length determined by carrier concentration profile simulations, localization length determined by ES-VRH-GD fits, and contact resistance found using the links and nodes model. Alumina-capped films: localization length determined by carrier concentration profile simulations and metallic grain size and contact resistance found by granular metal fits. Fitted parameter error corresponds to a 99.5% confidence interval. Error propagation calculations are shown in SI Text 4.

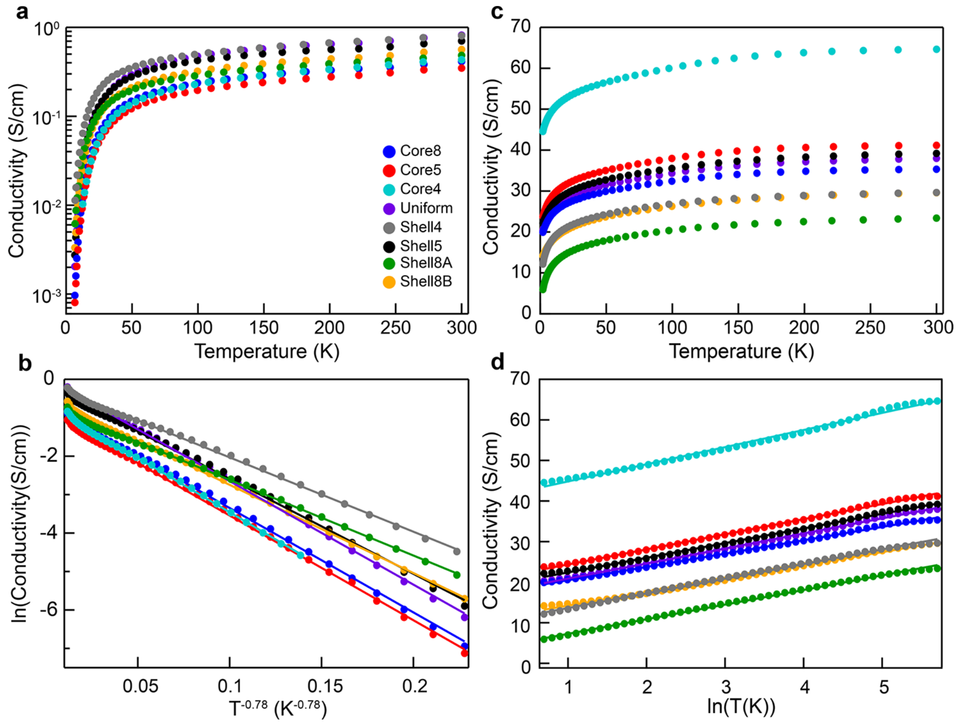

Figure 3. Temperature dependence of electron transport in bare (a,b) and alumina-capped (c,d) ITO NC films. Conductivity versus temperature (a) and Efros-Shklovskii variable range hopping with a Gaussian dispersion of energy levels fit for bare ITO NC films (b). Conductivity versus temperature (c) and granular metal conduction mechanism for alumina-capped ITO NC films (d). Markers indicate experimental data and lines show fits to ES-VRH-GD (b) and the granular metal (d) conduction mechanisms.

trend observed for the seven other samples. One possible explanation for this deviation may be Shell8B having a significantly lower overall dopant concentration. This explanation is supported by Shell8A having an increased overall dopant concentration with only modest changes to NC size and near surface dopant density, the conductivity increases nearly an order of magnitude and follows the predicted trend. However, the material-dependent constant, A, in the Miller-Abraham model and its dependence on dopant concentration are highly uncertain.[22−25] We refrain from analyzing the room temperature conductivity of bare films of Shell8B for this reason.

Comparing room-temperature conductivity of films is useful in determining the optimal material for a device but gives little insight into the differences in electron transport physics underlying these differences. Analysis of the underlying physics requires films to be viewed as a random resistor network composed of randomly positioned bonds, that is, conduction pathways, each with a finite resistance, R_{bond}. For NC films with much lower conductivity than their bulk analogue, bond resistance is approximately equal to the contact resistance, R_C, which describes the tunneling resistance between NCs,[16] and is calculated from the links and nodes model in three dimensions as

$$R_C \approx R_{\text{bond}} = \frac{(\varphi - \varphi_0)^{1.9}}{2\sigma r_0}$$

where σ is the film conductivity, φ is the NC volume fraction, φ_0 is the percolation threshold, and r_0 is the NC radius.[26,27] We assume the percolation threshold to be that of randomly packed

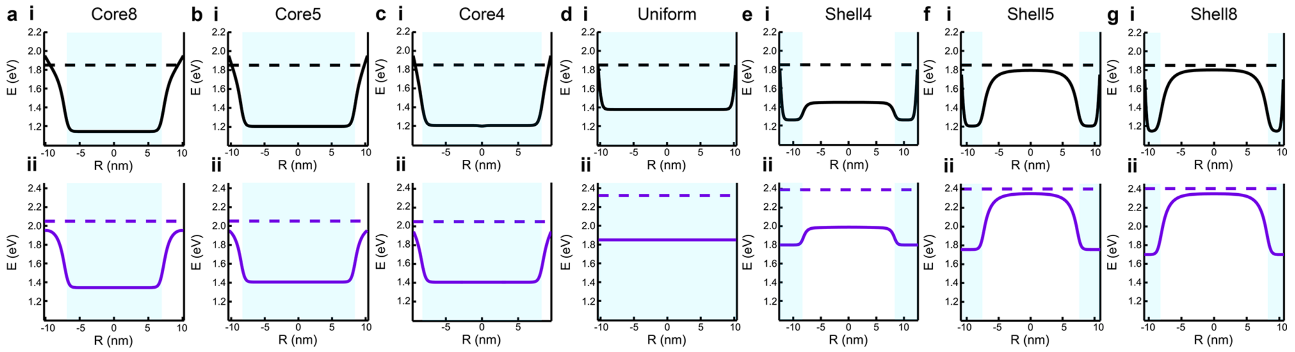

Figure 4. Simulated band profiles. Intra-NC band profile for Core8 (a), Core5 (b), Core4 (c), Uniform (d), Shell4 (e), Shell5 (f), and Shell8 (g) with a surface potential 0.2 eV below the flat band potential of indium oxide (a−g (i)) and equal to the flat band potential of the shell species (a−g (ii)). The latter represents the absence of surface-state induced depletion. In all cases, the horizontal dashed line is the Fermi level and the blue shaded region indicates the region of enriched dopants. $R = 0$ denotes the center of a NC and maximum $|R|$ denotes the surface.

spheres, approximately 0.2.[28] Inter-NC contact resistances are reported in Table 2. When R_C is greater than the critical tunneling resistance, which is determined by the ratio of charging energy to the mean energy spacing in a single grain, a material behaves as an insulator and conduction is dominated by a hopping mechanism (SI Text2).[29] R_C is well above the critical tunneling resistance for all NC films indicating that electrons must hop between NCs.

In films with no necking between NCs, R_C is primarily defined by a tunneling junction with resistance proportional to $\exp(s\sqrt{2m^* U_0}/\hbar)$ where s is the barrier width, U_0 is barrier height, m^* is the effective mass of an electron ($0.4m_e$ for ITO), and $\hbar$ is Planck's constant.[22] We use the magnitude of R_C as a metric to estimate the tunneling width. The barrier height, equal to the work function at the NC surface, is determined by the surface state energy due to Fermi level pinning and is assumed to be equal for all samples. One should note that this analysis is a simple estimate as the tunneling resistance has a pre-exponential factor that may have a dependence on overall dopant concentration or dopant distribution. However, it is clear from the order of magnitude difference in R_C between Shell8A and Core8 that NC dopant distribution significantly affects the tunneling barrier.

We performed variable-temperature conductivity measurements on the bare NC films to gain further insight on how intra-NC dopant profiles influence the inter-NC tunneling junctions (Figure 3a). Conductivity increases monotonically with increasing temperature for all films, characteristic of electrons conducting through a hopping mechanism. The temperature dependence of conductivity in an electron hopping regime is described by

$$\sigma(T) = \sigma_0 \exp\left(-\left(\frac{T_0}{T}\right)^m\right)$$

where σ_0 is treated as a material-dependent constant, T_0 is a characteristic temperature, and m depends on the specific hopping mechanism.[24] Zabrodskii analysis indicates m values of nearly 0.78 for all bare samples we measured (Figure S12).[30] Atypical values of m (those other than 0.25, 0.5, or 1) were investigated by Houtepen et al. and were explained by temporal broadening of energy levels within the density-of-states.[31] This broadening depends on the temperature dependence of heat capacity for the active material. Whereas Houtepen et al. assumed a constant heat capacity and found an m-value of 0.66, we used a power law fit to the ITO heat capacity ($C_p \propto CT^p$) to capture this temperature dependence in the model. Using this power-law heat capacity fit we derived the Efros-Shklovskii variable-range hopping with a Gaussian dispersion of energy levels (ES-VRH-GD) to have an m value of 0.78 (Figure S13, SI Text 3). The ES-VRH-GD characteristic temperature in this regime is then defined as

$$T_0 = \left(\frac{3.15e^4}{4\pi^2\varepsilon^2 k_B C a^2}\right)^{1/3}$$

where $C \approx 27$ is the heat capacity power-law coefficient for ITO, e is the electron charge, ε is the dielectric constant of the film, and a is the electron localization length. The film effective dielectric constant was calculated using methods developed by Reich and Shklovskii.[32] Here, the electron localization length defines the diameter of a sphere within which mobile electrons are confined at 0 K. Fits to variable temperature data and the corresponding localization lengths are reported in Figure 3b and Table 2, respectively. Fitting constants and error are reported in SI Text 4.

ES-VRH-GD fits to variable temperature conductivity data indicate the electron localization length increases as dopants move toward the surface. Core8 NC films exhibit a localization length nearly 3 nm smaller than the NC diameter while Shell4, Shell8A, and Shell8B show some degree of delocalization of electrons beyond the size of the NCs. The monotonic growth of localization length with increasing overall dopant concentration has been established as a signature of approaching the metal-insulator transition in NC films.[16,22,26] Interestingly, despite having the lowest overall dopant concentration, Shell8B shows a longer localization length than the core-doped and uniformly doped samples measured here. Previously, studies of the connection between localization and dopant concentration considered only films of uniformly doped NCs and those with passivated surfaces. Here we reveal that the more relevant property for bare NC films is the concentration of dopants in the near surface region. This is because greater (lesser) dopant density at the surface reduces (increases) the effects of surface depletion. Thus, films of low overall dopant concentration NCs can be engineered to produce a large localization length by controlling the dopant distribution.

To further understand the trend of localization length with changing dopant distribution, we simulated the band profiles within isolated ITO NCs with radially controlled dopant distribution in the presence of surface states that are approximated to be 0.2 eV below the conduction band minimum of indium oxide (Figure 4, SI Text 4, and Figure S14).[17] In uniformly doped ITO NCs (Figure 4di), the band profile is easily understood as a radial depletion region near the NC surface. When dopants are segregated, the band profile becomes significantly more complex. Tin dopants decrease the electronic band gap of indium oxide while also increasing the optical band gap due to state filling, that is, the Burstein−Moss effect.[33,34] This means that in addition to band bending at the surface, band bending will occur near the interface of doped and undoped regions within the NC. In core-doped ITO NCs (Figure 4a−ci), a relatively low density of charged defects near the surface results in a wide depletion region that extends to the doped core. In contrast, surface-doped ITO NCs (Figure 4d−gi) have a high density of charged defects near the surface, resulting in a sharper, narrower depletion region, which we have correlated with an expanded localization length in films fabricated from these NCs.

We simulated electron concentration profiles to visualize how these band profiles influence the electron localization length for each dopant distribution in a NC-NC tunneling junction (Figure 5a−g). The electron localization length is defined here as the diameter of a sphere containing all space with an electron concentration of greater than 10^{25} m^{-3}, the critical electron concentration for metallic behavior in ITO according to the Mott criterion.[35] Using this definition, we examine the electron localization compression due to depletion, which is simply the difference between the physical diameter of the NC and the electron localization length. As shown in Figure 5 a−c, the extended surface depletion region in core-doped samples leads to significant localization length shrinkage in Core8, Core5, and Core4 of 2.6, 1.6, and 0.7 nm, respectively. For uniform dopant distribution (Figure 5d), the localization length is compressed only slightly at about 0.4 nm. Finally, when the majority of dopants are near the surface (Figure 5e−g), the localization volume is approximately the size of the NC with Shell5 having 0.1 nm compression and Shell4 and Shell8 being fully delocalized within the NC. Shell4 achieves full delocalization whereas Shell5 does not due to the larger diameter of Shell4. The definition of electron localization length in our simulations is simplified by ignoring wave function decay beyond the metallic region of the NC. Despite this, the trend observed in simulations is mirrored in localization lengths determined by analysis of variable temperature conductivity data (Table 2). Without considering wave function decay beyond the physical NC dimensions our simulation cannot describe electron localization lengths greater than the NC diameter; however, the simulated intra-NC electron concentration profiles for Shell4 and Shell8 agree with the possibility for electron delocalization outside of the NC, as suggested by the experimental variable temperature conductivity data.

The importance of the localization length and its magnitude relative to the NC size is apparent as we return to analyze the limiting factors in achieving high conductivity NC films. The contact resistance, analyzed as a tunneling junction, is $R_C \propto \exp(s\sqrt{2m^*U_0}/\hbar)$. Again, s defines the separation between the edges of electron localization volumes. Using a simple model of two NCs in contact at a point, and electronically connected by a tunnel junction due to depletion, s is simply the electron localization compression discussed above (Figure 5). From our analysis, as the dopant profile

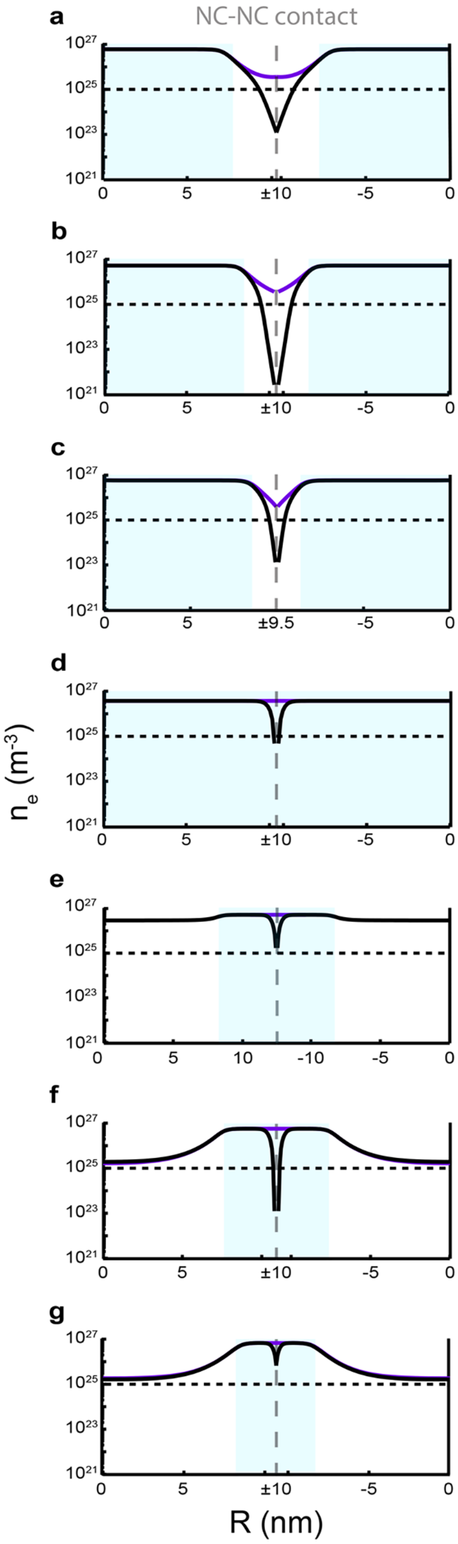

Figure 5. Simulated electron concentration profiles. Radial electron concentration profile for Core8 (a), Core5 (b), Core4 (c), Uniform (d), Shell4 (e), Shell5 (f), and Shell8 (g) with a surface potential 0.2 eV below the flat band potential of indium oxide (black) and equal to the flat band potential of the shell species (purple). Vertical dashed line is where neighboring NCs touch and horizontal dashed line is the critical carrier concentration. In all cases, the blue shaded region indicates the region of enriched dopants. $R = 0$ denotes the center of a NC and maximum |R| denotes the surface.

moves toward the surface, there is monotonic decrease in s. This diminished barrier width implies a decrease in contact resistance, in agreement with experimental results for Core8 through Shell8A.

Alumina-Capped Films. Following alumina deposition, the conductivity of all films increased significantly as shown in Figure 2. All capped-NC films exhibit nearly identical conductivity. We performed variable temperature conductivity measurements on NC films after alumina capping to gain insight on electron transport barriers (Figure 3c). While conductivity of alumina-capped films increases monotonically with increasing temperature for all films, conductivity is consistent with a logarithmic dependence on temperature. Conduction of this type has been observed in granular ITO thin films and is ascribed to a granular metal conduction mechanism.[36−38] We note that while hopping conduction is a description of electrons overcoming a Coulombic blockage by undergoing hops of temporally varying distances, the granular metal conduction model describes the competition between Coulombic barriers and NC-NC coupling. Granular metal conduction depends on the grain (NC) size and the degree of coupling, reflected in tunneling conductance between neighboring NCs, rather than the electron localization length. The temperature dependence of conductivity in granular metals is described by

$$\sigma = \sigma_0\left(1 + \frac{1}{2\pi g_T d}\ln\left(\frac{k_B T}{g_T E_C}\right)\right)$$

where $\sigma_0 = g_T\left(\frac{2e^2}{\hbar}\right)\alpha^{2-d}$, g_T is the nondimensional tunneling conductance between grains, α is the grain diameter, d is the system dimensionality, and $E_C = \frac{e^2}{2\pi\varepsilon\alpha}$ is the charging energy of a grain.[29,36] Metallic grain size and tunneling conductance were calculated from the slope and intercept, respectively, of σ versus $\ln(T)$ as shown in Figure 3d. Metallic grain size and tunneling conductance are reported in Table 2. Fitting constants and error are reported in SI Text 4. This model is valid for all films measured as the tunneling conductance is below the intra-NC conductance and above the critical tunneling conductance, the inverse of the previously discussed critical tunneling resistance, and all fitted temperatures are above the quantum limit (SI Text 6).

The grain size in ITO NC films with alumina capping does not show a clear dependence on dopant distribution as localization length did in bare films but rather becomes approximately equal to the NC diameter for all samples based on granular metal fits of variable temperature conductivity data. Simulated band profiles for passivated surface ITO NCs (Figure 4a−g(ii)) show the electron concentration exceeds the critical value throughout the NCs despite the presence of the core−shell interface band bending. Shell- and uniformly doped NCs (Figure 4d−g(ii)) show a flat band on the surface while in core-doped NCs the accumulation region from the core has not yet reached flat band at the NC surface (Figure 4a−c(ii)). Examination of electron concentration profiles (Figure 5) provides an explanation for the experimental observation that grain size does not show a clear dependence of dopant distribution. As shown in the figure, the localization length expands upon passivation of the surface, eliminating the separation between electron localization volumes (Figure 5). NC localization volumes are now metallic spheres touching via point contacts, which have a significantly lower contact resistance due to a decreased tunneling barrier width. Dopant profile dependence is observed in neither grain size nor contact resistance following surface passivation by ALD.

In conclusion, dopant distribution within NCs was shown to be an effective means to influence the electronic properties of bare ITO NC films (including overall conductivity, contact resistance, and electron localization length) at a constant overall tin concentration. These effects were understood largely based on the varying effects of dopant distribution on the near-surface depletion layer. The model typically used to analyze variable temperature conductivity assumes full dopant ionization and uniform electron distribution within NCs, which is obviously not a fully physical description of our materials. However, no established theories describing electron conduction through NC films explicitly incorporate the potential for dopant segregation or intra-NC band bending. The assumptions of uniform electron distribution and full dopant ionization create some uncertainty in the meaning of the ES-VRH-GD derived localization length. However, considering the localization lengths derived from simulated electron concentration profiles agree well with the values derived from these fits to the experimental data suggests that any error caused by these assumptions is small compared to the influence of dopant segregation on transport properties. Conclusions drawn here should be viewed as a general case for doped semiconductors in the presence of surface states as our simulations and their interpretations are applicable across a range of systems.

We have examined the influence of dopant distribution within ITO NCs on the conductivity of NC films while also considering the presence of surface defects and the potential to passivate surface defects using ALD. Intra-NC dopant distribution plays a strong role in determining macroscopically observable electronic properties, such as film conductivity, and microscopic electronic properties, such as localization length and contact resistance, of bare NC films. The influence of dopant distribution on the properties listed above is the result of modulating surface depletion as these effects are eliminated following the deposition of alumina. These experimental results were supported by simulations of intra-NC band profiles, which showed identical trends in electron localization and its implications on contact resistance. Dopant distribution engineering offers a promising route through surface modification to improve the conductivity of NC films for device applications. Using intra-NC dopant distribution to tune surface depletion additionally creates interesting new avenues of study regarding phenomena and applications that depend on the interaction between the conduction electrons and the surrounding environments such as electrochromic devices, plasmonics materials, sensors, and catalysts.

■ ASSOCIATED CONTENT

Ⓢ Supporting Information

The Supporting Information is available free of charge on the ACS Publications website at DOI: 10.1021/acs.nanolett.7b05484.

Details of nanocrystal synthesis, nanocrystal characterization (STEM and XRD), film characterization (XPS, IR, and visible spectroscopy, EP, alumina-capped SEM, TOF-SIMS, and air stability), conduction mechanism details (air stability, critical tunneling resistance, Zabrodskii analysis, heat capacity fit, derivation of

Efros−Shklovskii variable range hopping with Gaussian broadening of energy levels, fitting constants error analysis, and granular metal model validity), and details of band profile simulations (PDF)

AUTHOR INFORMATION

Corresponding Author

*E-mail: milliron@che.utexas.edu. Telephone: (512) 232-5702.

ORCID

Ankit Agrawal: 0000-0001-7311-7873
Delia J. Milliron: 0000-0002-8737-451X

Notes

The authors declare no competing financial interest.

ACKNOWLEDGMENTS

This research was supported by the National Science Foundation (NSF), including NASCENT, an NSF ERC (EEC-1160494, C.M.S.), CHE-1609656 (A.A.), the University of Texas at Austin MRSEC (DMR-1720595), the University of Minnesota MRSEC (DMR-1420013; Z.L.R., B.L.G., U.R.K.), a Graduate Research Fellowship under Award Number (DGE-1610403, S.L.G.), and the Welch Foundation (F-1848). This work was performed in part at the Molecular Foundry, Lawrence Berkeley National Laboratory, which is supported by the Office of Science, Office of Basic Energy Sciences, of the U.S. Department of Energy (DOE) under Contract No. DE-AC02-05CH11231. S.D.L. was supported by a DOE Early Career Research Program grant to D.J.M.

REFERENCES

(1) Barquinha, P.; Martins, R.; Pereira, L.; Fortunato, E. *Transparent Oxide Electronics*; John Wiley & Sons, Ltd: Chichester, UK, 2012.

(2) Ellmer, K. Past Achievements and Future Challenges in the Development of Optically Transparent Electrodes. *Nat. Photonics* **2012**, *6*, 809.

(3) Kim, J.-Y.; Kotov, N. A. Charge Transport Dilemma of Solution-Processed Nanomaterials. *Chem. Mater.* **2014**, *26*, 134−152.

(4) Pham, H. T.; Jeong, H.-D. Newly Observed Temperature and Surface Ligand Dependence of Electron Mobility in Indium Oxide Nanocrystals Solids. *ACS Appl. Mater. Interfaces* **2015**, *7*, 11660−11667.

(5) Zarghami, M. H.; Liu, Y.; Gibbs, M.; Gebremichael, E.; Webster, C.; Law, M. P-Type PbSe and PbS Quantum Dot Solids Prepared with Short-Chain Acids and Diacids. *ACS Nano* **2010**, *4*, 2475−2485.

(6) Miller, A.; Abrahams, E. Impurity Conduction at Low Concentrations. *Phys. Rev.* **1960**, *120*, 745−755.

(7) Talapin, D. V.; Lee, J.-S.; Kovalenko, M. V.; Shevchenko, E. V. Prospects of Colloidal Nanocrystals for Electronic and Optoelectronic Applications. *Chem. Rev.* **2010**, *110*, 389−458.

(8) Zabet-Khosousi, A.; Dhirani, A.-A. Charge Transport in Nanoparticle Assemblies. *Chem. Rev.* **2008**, *108*, 4072−4124.

(9) Talapin, D. V.; Murray, C. B. PbSe Nanocrystal Solids for N- and p-Channel Thin Film Field-Effect Transistors. *Science* **2005**, *310*, 86−89.

(10) Liu, W.; Lee, J.-S.; Talapin, D. V. III−V Nanocrystals Capped with Molecular Metal Chalcogenide Ligands: High Electron Mobility and Ambipolar Photoresponse. *J. Am. Chem. Soc.* **2013**, *135*, 1349−1357.

(11) Garcia, G.; Buonsanti, R.; Runnerstrom, E. L.; Mendelsberg, R. J.; Llordes, A.; Anders, A.; Richardson, T. J.; Milliron, D. J. Dynamically Modulating the Surface Plasmon Resonance of Doped Semiconductor Nanocrystals. *Nano Lett.* **2011**, *11*, 4415−4420.

(12) Liu, Y.; Tolentino, J.; Gibbs, M.; Ihly, R.; Perkins, C. L.; Liu, Y.; Crawford, N.; Hemminger, J. C.; Law, M. PbSe Quantum Dot Field-Effect Transistors with Air-Stable Electron Mobilities above 7 Cm2 V−1 S−1. *Nano Lett.* **2013**, *13*, 1578−1587.

(13) Thimsen, E.; Johnson, M.; Zhang, X.; Wagner, A. J.; Mkhoyan, K. A.; Kortshagen, U. R.; Aydil, E. S. High Electron Mobility in Thin Films Formed via Supersonic Impact Deposition of Nanocrystals Synthesized in Nonthermal Plasmas. *Nat. Commun.* **2014**, *5*, 5822.

(14) Ephraim, J.; Lanigan, D.; Staller, C.; Milliron, D. J.; Thimsen, E. Transparent Conductive Oxide Nanocrystals Coated with Insulators by Atomic Layer Deposition. *Chem. Mater.* **2016**, *28*, 5549−5553.

(15) Liu, Y.; Gibbs, M.; Perkins, C. L.; Tolentino, J.; Zarghami, M. H.; Bustamante, J.; Law, M. Robust, Functional Nanocrystal Solids by Infilling with Atomic Layer Deposition. *Nano Lett.* **2011**, *11*, 5349−5355.

(16) Greenberg, B. L.; Robinson, Z. L.; Reich, K. V.; Gorynski, C.; Voigt, B. N.; Francis, L. F.; Shklovskii, B. I.; Aydil, E. S.; Kortshagen, U. R. ZnO Nanocrystal Networks Near the Insulator−Metal Transition: Tuning Contact Radius and Electron Density with Intense Pulsed Light. *Nano Lett.* **2017**, *17*, 4634.

(17) Zandi, O.; Agrawal, A.; Shearer, A. B.; Gilbert, L. C.; Dahlman, C. J.; Staller, C. M.; Milliron, D. J. Impacts of Surface Depletion on the Plasmonic Properties of Doped Semiconductor Nanocrystals. **2017**, arXiv:1709.07136 [physics.optics].

(18) Jansons, A. W.; Hutchison, J. E. Continuous Growth of Metal Oxide Nanocrystals: Enhanced Control of Nanocrystal Size and Radial Dopant Distribution. *ACS Nano* **2016**, *10*, 6942−6951.

(19) Hewitt, R. W.; Winograd, N. Oxidation of Polycrystalline Indium Studied by X-Ray Photoelectron Spectroscopy and Static Secondary Ion Mass Spectroscopy. *J. Appl. Phys.* **1980**, *51*, 2620−2624.

(20) Kang, M. S.; Sahu, A.; Norris, D. J.; Frisbie, C. D. Size-Dependent Electrical Transport in CdSe Nanocrystal Thin Films. *Nano Lett.* **2010**, *10*, 3727−3732.

(21) Liu, Y.; Gibbs, M.; Puthussery, J.; Gaik, S.; Ihly, R.; Hillhouse, H. W.; Law, M. Dependence of Carrier Mobility on Nanocrystal Size and Ligand Length in PbSe Nanocrystal Solids. *Nano Lett.* **2010**, *10*, 1960−1969.

(22) Chen, T.; Reich, K. V.; Kramer, N. J.; Fu, H.; Kortshagen, U. R.; Shklovskii, B. I. Metal-Insulator Transition in Films of Doped Semiconductor Nanocrystals. *Nat. Mater.* **2016**, *15*, 299.

(23) Arginskaya, N. V.; Kozub, V. I. Potential Influence of Pre-Exponential Factors on the Temperature Dependence of Variable-Range Hopping Conductivity. *Sov. J. Exp. Theor. Phys.* **1994**, *79*, 466−472.

(24) Shklovskii, B. I.; Efros, A. L. *Electronic Properties of Doped Semiconductors*; Springer-Verlag: Berlin Heidelberg GmbH.

(25) Yildiz, A.; Serin, N.; Serin, T.; Kasap, M. Crossover from Nearest-Neighbor Hopping Conduction to Efros−Shklovskii Variable-Range Hopping Conduction in Hydrogenated Amorphous Silicon Films. *Jpn. J. Appl. Phys.* **2009**, *48*, 111203.

(26) Lanigan, D.; Thimsen, E. Contact Radius and the Insulator−Metal Transition in Films Comprised of Touching Semiconductor Nanocrystals. *ACS Nano* **2016**, *10*, 6744−6752.

(27) Shklovskiĭ, B. I.; Éfros, A. L. Percolation Theory and Conductivity of Strongly Inhomogeneous Media. *Sov. Phys. Uspekhi* **1975**, *18*, 845.

(28) Powell, M. J. Site Percolation in Randomly Packed Spheres. *Phys. Rev. B: Condens. Matter Mater. Phys.* **1979**, *20*, 4194−4198.

(29) Beloborodov, I. S.; Lopatin, A. V.; Vinokur, V. M. Universal Description of Granular Metals at Low Temperatures: Granular Fermi Liquid. *Phys. Rev. B: Condens. Matter Mater. Phys.* **2004**, *70*, 205120.

(30) Zabrodskii, A. G. The Coulomb Gap: The View of an Experimenter. *Philos. Mag. B* **2001**, *81*, 1131−1151.

(31) Houtepen, A. J.; Kockmann, D.; Vanmaekelbergh, D. Reappraisal of Variable-Range Hopping in Quantum-Dot Solids. *Nano Lett.* **2008**, *8*, 3516−3520.

(32) Reich, K. V.; Shklovskii, B. I. Dielectric Constant and Charging Energy in Array of Touching Nanocrystals. *Appl. Phys. Lett.* **2016**, *108*, 113104.

(33) Berggren, K.-F.; Sernelius, B. E. Band-Gap Narrowing in Heavily Doped Many-Valley Semiconductors. *Phys. Rev. B: Condens. Matter Mater. Phys.* **1981**, *24*, 1971−1986.

(34) Hamberg, I.; Granqvist, C. G.; Berggren, K.-F.; Sernelius, B. E.; Engström, L. Band-Gap Widening in Heavily Sn-Doped In_2O_3. *Phys. Rev. B: Condens. Matter Mater. Phys.* **1984**, *30*, 3240−3249.

(35) Mott, N. F. Conduction in Non-Crystalline Systems. *Philos. Mag.* **1968**, *17*, 1259−1268.

(36) Beloborodov, I. S.; Lopatin, A. V.; Vinokur, V. M.; Efetov, K. B. Granular Electronic Systems. *Rev. Mod. Phys.* **2007**, *79*, 469−518.

(37) Lin, J.-J.; Li, Z.-Q. Electronic Conduction Properties of Indium Tin Oxide: Single-Particle and Many-Body Transport. *J. Phys.: Condens. Matter* **2014**, *26*, 343201.

(38) Zhang, Y.-J.; Li, Z.-Q.; Lin, J.-J. Logarithmic Temperature Dependence of Hall Transport in Granular Metals. *Phys. Rev. B: Condens. Matter Mater. Phys.* **2011**, *84*, 052202.